

This is the accepted manuscript made available via CHORUS. The article has been published as:

## Separability of math

$$\text{mrow} > \text{msub} > \text{mi mathvariant="normal"} > \text{H} / \text{mi} > \text{mn} > 2 / \text{mn} > \text{msub} > \text{mi mathvariant="normal"} > \text{O} / \text{mi} > \text{mrow} > \text{/math}$$
  
molecular potential surfaces in hyperspherical coordinates  
via adiabatic approximation

Jiří Daněk and C. D. Lin

Phys. Rev. A **102**, 042809 — Published 12 October 2020

DOI: [10.1103/PhysRevA.102.042809](https://doi.org/10.1103/PhysRevA.102.042809)

# On separability of $\text{H}_2\text{O}$ molecular potential surfaces in hyperspherical coordinates via adiabatic approximation

Jiří Daněk\* and C. D. Lin†

Department of Physics, Kansas State University, Manhattan, Kansas 66506, USA

(Dated: September 6, 2020)

An adiabatic scheme for separation of the three-dimensional nuclear dynamics on the ground electronic Born-Oppenheimer potential energy surface of an  $\text{H}_2\text{O}$  molecule in hyperspherical coordinates is presented. It is found that the three vibrational modes are weakly coupled and the 3D vibrational wave function can be approximated as a product of three separable functions: one represented by the hyperradius and two by the two hyperangles individually. This framework is then used for investigation of the formation and the role of a saddle-like barrier arising in the two hyperspherical angles that is to moderate the  $\text{OH} + \text{H}$  dissociation process. In order to test the validity of the framework, vibrational states with energies up to  $19\ 500\ \text{cm}^{-1}$  are constructed under the assumptions of adiabaticity and separability and compared to full three-dimensional high precision numerical calculations yielding remarkable correspondence. As a result we present a simple construction scheme for separated molecular vibration states as the first step towards theoretical investigation of laser-driven molecular dynamics of triatomic molecules.

## INTRODUCTION

With the rapid development of laser technology, femtosecond and even attosecond experimental techniques in the recent years [1–3], the need for comprehensible theoretical models of molecular vibrational states which take part in the dynamics grows. Although various *ab initio* quantum calculation packages allow fast calculation of normal modes and their frequencies, determination of higher vibrational states and their energies still requires knowledge of the potential energy surface (PES) and solution of full-dimensional time-independent Schrödinger equation. The difficulty owes much to the increasing number of internal degrees of freedom of a molecule which grows as  $3N - 5$  for linear molecules and  $3N - 6$  for non-linear molecules, where  $N$  is the number of atoms in the molecule. Clearly a full-dimensional quantum mechanical numerical solution is prohibitively complicated. The second complication presents the separability of the vibrational states into modes which is directly connected with suitable choice of coordinate system. While quantum mechanical numerical solution can be, in principle, obtained in any coordinates, the states may not exhibit any clear nodal structure required for unambiguous identification of modes and assignment of quantum numbers.

Separability of vibrational modes can significantly simplify dynamical nuclear problems, e.g., due to symmetry reasons. Standard and attractive approximation for complex molecules is to freeze all the degrees of freedom except for one interatomic pair or an angle between two such pairs. This avoids the treatment of a multi-dimensional surface and the analysis of the dynamics can be dramatically simplified. On the other hand, such simplification may occur in several distinct regions of the

multi-dimensional potential surface only, such that connecting such regions in a time-dependent way is needed. Before such an approach can be established, however, it is critical that one can identify the circumstance where dynamics in a multi-dimensional potential surface can be simplified, preferable as separable components. For this purpose, we aim at examining the ground state potential surface of water molecules ( $\text{H}_2\text{O}$ ), with the goal of identifying the separability of the nuclear degrees of freedom.

Over the years, several models for the nuclear vibrations of  $\text{H}_2\text{O}$  have been formulated. The initial attempt assumed only small displacements of atoms from their equilibrium position so that the molecular potential expanded at the equilibrium could be diagonalized alongside with the kinetic term giving rise to the well known normal modes (see, e.g., [4]). The normal modes, however, experience various mixings: Fermi [5] at lower energies and Darling-Dennison [6] at high energies. Moreover, the anharmonicity of the potential had to be taken into account by correcting terms [7]. Later it was shown that the so called local-mode model provides an overall better fit to vibration energies (see, e.g., Review [8] and references therein). Nevertheless, the local mode description fails for the lower vibration states due to the relatively small mass of the Oxygen atom and yields a good agreement only from the fourth polyad on [9]. Moreover, for water molecule not all normal modes get washed out due to the Darling-Dennison mixing and some survive alongside the local modes up to high energies [10].

Hyperspherical modes offered an alternative to the two presented types of modes giving rise to various methods for hyperspherical modes determination based on adiabatic approximation (e.g., see Review [11] and reference therein) or assume mode separability in the self-consistent field approach [12]. Selective dissociation through hyperspherical modes was investigated in [13–16] and adiabatic separability of stretching and bending modes in Radau and valence coordinates was addressed in [17].

---

\* danekj@phys.ksu.edu

† cdlin@phys.ksu.edu

New era in the theoretical spectroscopy of  $\text{H}_2\text{O}$  came with precise ab initio calculations of molecular potential energy surface (PES) [18–26] which allowed to calculate line lists for  $\text{H}_2\text{O}$  with high precision up to 41 000  $\text{cm}^{-1}$  and  $J = 72$  [27]. These listed PES are either constructed completely from ab initio calculations or use them as a starting surface which then is fine-morphed to fit available spectroscopic data. As we have already mentioned, both normal-mode and local-mode based methods offer a unique insight into the internal dynamics of molecules.

In this work, we investigate the separability of the PES of  $\text{H}_2\text{O}$  molecule from [28] in hyperspherical coordinates [29]. We use the adiabatic approximation to separate the motion associated with the symmetrical stretch from the motions in two hyperangles associated with bending and antisymmetric stretching modes. Further, we separate the motion in the two hyperangular coordinates resulting eventually in three independent 1D Schrödinger equations. As one of our results, we reconstruct the full 3D states within our separability assumption and benchmark the found energies against high-precision numerical results from [30]. The goal of this work is to construct separated vibration states with trivially given symmetry and quantum numbers reasonably resembling the real vibration states and energies with lowest effort possible. We regard development of such a framework as an essential step towards theoretical investigation of strong-field processes in triatomic molecules. Especially, we hope that the hyperspherical coordinates will help us in the future to shed light on selective dissociation limit for water isotopomers (e.g., HOD) as they lose the molecular symmetry. In such case the bond between the diatomic remnants will play a crucial role and is well described within one of the sets which we will introduce later.

The paper is structured as follows: in Sec. I we introduce the hyperspherical coordinates via three different sets of Jacobi coordinates and show how the  $\text{H}_2\text{O}$  molecule and PES behave in these coordinates. Further in that section, we transform the Hamiltonian in hyperspherical coordinates. We further introduce grand angular momentum operator and analyze the modes given in hyperspherical coordinates. The adiabatic approximation and decomposition of the 3D Hamiltonian in hyperspherical coordinates into two parts is discussed in Sec. II. Moreover, all non-adiabatic correction terms are derived and a way is shown how to solve the adiabatic 2D Hamiltonian with B-Spline basis functions. In Sec. III we discuss the main novelty of this work: possible separability of the PES in the current hyperspherical coordinates. In the course of this action the 2D vibration wave functions are constructed in the separability approximation and analyzed. Their role in the  $\text{OH} + \text{H}$  dissociation process is also discussed. The full separability of the 3D PES in all three hyperspherical coordinates is addressed in Sec. IV where the total energies are calculated in the adiabatic approximation neglecting non-adiabatic corrections and compared to full 3D numerical calculations. Finally, the results are discussed and concluded in Sec. V. A deeper

analysis of the atomic displacements associated with the hyperspherical modes is provided in Appendix A. Atomic units are used thorough the text unless stated otherwise.

## I. FORMULATION IN HYPERSPHERICAL COORDINATES

### A. Mass-scaled hyperspherical coordinates

Internal degrees of freedom for the triatomic  $\text{H}_2\text{O}$  molecule can be described by Jacobi vectors in three different ways as shown in Fig. 1. The first Jacobi vector  $\rho_1$  always points from one atom to another whereas the second vector  $\rho_2$  from the center-of-mass of the two atoms to the third one.

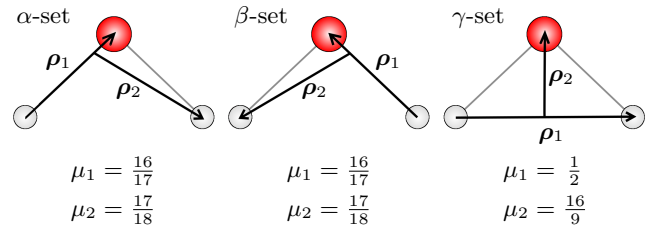


FIG. 1. Demonstration of the three ways for defining Jacobi vectors with corresponding reduced masses  $\mu_1$  and  $\mu_2$ .

Further, it is common to introduce mass-weighted Jacobi coordinates as

$$\xi_1 = \sqrt{\frac{\mu_1}{\mu}} \rho_1, \quad \xi_2 = \sqrt{\frac{\mu_2}{\mu}} \rho_2, \quad (1)$$

with an arbitrary parametric mass  $\mu$  and reduced masses as

$$\begin{aligned} \mu_1 &= \frac{m_a m_b}{m_a + m_b}, \\ \mu_2 &= \frac{(m_a + m_b) m_c}{m_a + m_b + m_c}, \end{aligned} \quad (2)$$

where indices a, b and c depend on the set of Jacobi coordinates. The masses in  $\mu_1$  are the masses of the atoms connected by  $\rho_1$  and the third remaining mass in  $\mu_2$  is the mass of the last atom.

The hyperspherical coordinates can be defined in several ways but we will follow the definition from [29] yielding

$$\begin{aligned} R &= \sqrt{\xi_1^2 + \xi_2^2}, \\ \phi &= \text{atan} \frac{\xi_2}{\xi_1}, \\ \theta &= \text{acos} \frac{\xi_1 \cdot \xi_2}{\xi_1 \xi_2}. \end{aligned} \quad (3)$$

Although the values of  $\phi$  and  $\theta$  vary when transforming between the sets, the value  $R$  is identical for all three sets. Configurations of the molecule with respect to the

angles  $\phi$  and  $\theta$  are shown in Fig. 2. The figures are carried out for a constant value of  $R$  but are valid for any value of the hyperradius. The hyperradius is connected only to the overall size of the molecule and does not change the internal angles nor the ratio between the two bond lengths used for determination of the dissociation regions. In this work we set  $\mu = \mu_2$  from the  $\gamma$ -set, which sets the minimum of the potential to hyperradius  $R = 1.881$  a.u. and to hyperangles  $\phi = 45.52^\circ$  and  $\theta = 72.32^\circ$  for both  $\alpha$ - and  $\beta$ -set and to hyperangles  $\phi = 36.15^\circ$  and  $\theta = 90^\circ$  for  $\gamma$ -set. The global minimum is marked by a cross in each of the panels in Fig. 2.

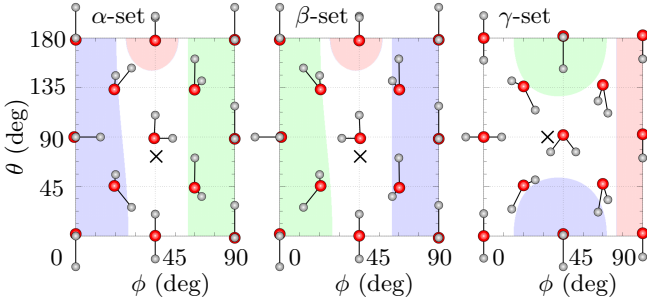


FIG. 2. Configuration of the molecule (HOH) at a constant hyperradius  $R$  with respect to hyperspherical coordinates  $\phi$  and  $\theta$  and the choice of set. The second Jacobi vector is always oriented along  $\theta$ -axis. Position of the global minimum is marked with black cross. The shaded regions indicate which atom is the furthest from the others: in blue region it is the first hydrogen ( $H+OH$ ), in red region the oxygen ( $H_2+O$ ) and in green region the second hydrogen ( $HO+H$ ).

The PES of  $H_2O$  molecule possesses only one global minimum which is also called equilibrium. Nevertheless, it is of interest to have a look at position of minimum in each slice of PES with respect to hyperradius as we do in Fig. 3. The global minimum is marked by black cross and lies on purple curve which marks the position of minimum of 2D PES slice of constant  $R$ . Remarkably, position of the minimum manifest a split starting at  $R \approx 2.4$ . Since the  $\alpha$ -set does not exploit the molecular symmetry, the split minima are located at distinct hyperangles  $\phi$  and  $\theta$  as the figure shows. This is different for the  $\gamma$ -set, which reflects the molecular symmetry. In this set, both split minima are located at the same value of hyperangle  $\phi$  and their position in hyperangle  $\theta$  respects the axis of symmetry  $\theta = 90^\circ$ . We will discuss later in the text how this bifurcation point is connected to two dissociation channels  $OH + H$ .

## B. Molecular Hamiltonian

The molecular Hamiltonian in Cartesian coordinates  $\mathbf{x}_i$  of the  $i$ th nucleus yields

$$\hat{H} = \sum_{i=1}^3 -\frac{1}{2m_i} \nabla^2(\mathbf{x}_i) + V, \quad (4)$$

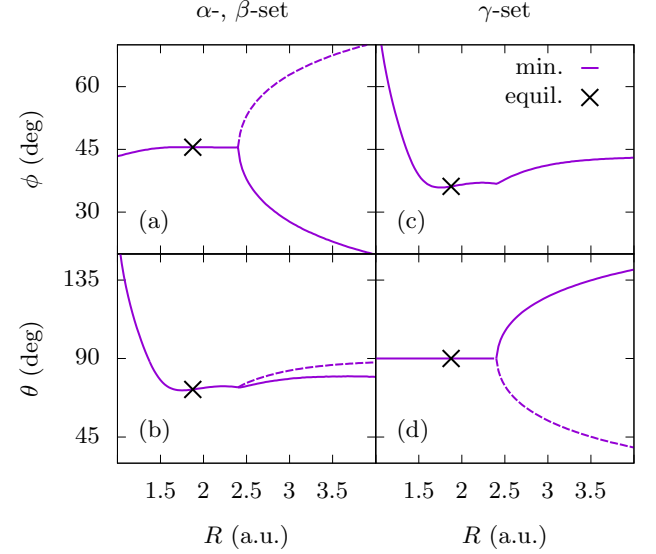


FIG. 3. Position of the minima in slices of the potential, i.e.,  $V(R = \text{const.}, \phi, \theta)$ , in hyperspherical coordinates with respect to  $R$  are projected and marked with magenta lines for  $\alpha$ - and  $\beta$ -set in panels (a) and (b) and for  $\gamma$ -set in panels (c) and (d). The position of the global minimum is marked with black cross. We can see that the minimum of the potential splits at  $R \approx 2.4$  and two minima are created (denoted with full and dashed line). In  $\alpha$ -,  $\beta$ -set, both minima are located at different hyperangles. In  $\gamma$ -set, the two minima are located at the same hyperangle  $\phi$  and in hyperangle  $\theta$  they respect the symmetry axis  $\theta = 90^\circ$ . Let us also remark that the two minima interchange under transformations between  $\alpha$ - and  $\beta$ -set.

with potential  $V$  accounting for the electronic energy and nuclear repulsion energy. For three atoms, in Jacobi coordinates, the ro-vibrational Hamiltonian simplifies to [31, 32]

$$\hat{H}' = \hat{K}_{vr} + \hat{K}_v + V(\rho_1, \rho_2, \theta), \quad (5)$$

where

$$\begin{aligned} \hat{K}_{vr} &= \frac{1}{2} \left[ \frac{1}{\mu_2 \rho_2^2} (\Pi_x^2 + \Pi_y^2) + \left( \frac{\text{cosec}^2 \theta}{\mu_1 \rho_1^2} + \frac{\cot^2 \theta}{\mu_2 \rho_2^2} \right) \Pi_z^2 \right. \\ &\quad \left. + \frac{\cot \theta}{\mu_2 \rho_2^2} (\Pi_x \Pi_z + \Pi_z \Pi_x) \right] - \frac{i}{\mu_2 \rho_2^2} \left( \frac{\partial}{\partial \theta} + \frac{\cot \theta}{2} \right) \Pi_y, \\ \hat{K}_v &= -\frac{1}{2\mu_1 \rho_1^2} \frac{\partial}{\partial \rho_1} \left( \rho_1^2 \frac{\partial}{\partial \rho_1} \right) - \frac{1}{2\mu_2 \rho_2^2} \frac{\partial}{\partial \rho_2} \left( \rho_2^2 \frac{\partial}{\partial \rho_2} \right) \\ &\quad - \frac{1}{2} \left( \frac{1}{\mu_1 \rho_1^2} + \frac{1}{\mu_2 \rho_2^2} \right) \frac{1}{\sin \theta} \frac{\partial}{\partial \theta} \left( \sin \theta \frac{\partial}{\partial \theta} \right). \end{aligned} \quad (6)$$

The terms  $\hat{K}_{vr}$  and  $\hat{K}_v$  represent the rovibrational and vibration part of the Hamiltonian, respectively. The quantity  $\Pi_\alpha$  are the total angular momentum operators which depend on the Euler angles in such a way that the components of the total angular momentum in  $\rho_i$  can be obtained from matrix multiplication

$$\mathbf{L} = -\mathbf{C} \mathbf{\Pi}. \quad (7)$$

The volume element for the internal coordinates yields  $dV = \rho_1^2 \rho_2^2 \sin \theta d\rho_1 d\rho_2 d\theta$  and for the Euler angle part it depends on the sine of the second Euler angle. For further details about Jacobi coordinates in the embedded body frame see [31].

From now on, we will concentrate only on the vibrational kinetic term of the Hamiltonian  $\hat{K}_v$  which yields in hyperspherical coordinates

$$\hat{K}_v = -\frac{1}{2\mu} \frac{\partial^2}{\partial R^2} + \frac{\Lambda^2 - \frac{1}{4}}{2\mu R^2}, \quad (8)$$

with the squared grand angular momentum operator

$$\Lambda^2 = -\frac{\partial^2}{\partial \phi^2} - \frac{1}{\sin^2 \phi \cos^2 \phi \sin \theta} \frac{\partial}{\partial \theta} \left( \sin \theta \frac{\partial}{\partial \theta} \right). \quad (9)$$

Let us note that in the calculation the wave function was rescaled by a factor of  $R^{5/2} \sin \phi \cos \phi$  and the volume element now becomes  $dV = \sin \theta dR d\phi d\theta$ . Let us also remark that transformation of the wave function from hyperspherical to Cartesian coordinates can be performed simply by removing the scaling factor.

### C. Hyperspherical and normal modes

It is reasonable to exploit the trivial symmetry of the water molecule and connect the two hydrogen atoms with the first Jacobi vector, which we call  $\gamma$ -set for conventional reasons. Reduced masses in such case yield

$$\mu_1 = \frac{m_H}{2}, \quad \mu_2 = \frac{4\mu_1 m_O}{4\mu_1 + m_O}. \quad (10)$$

The Jacobi vectors can be fixed in the embedded body frame following [31] as

$$\rho_1 = \rho_1 \begin{pmatrix} \sin \theta \\ 0 \\ \cos \theta \end{pmatrix}, \quad \rho_2 = \rho_2 \begin{pmatrix} 0 \\ 0 \\ 1 \end{pmatrix}, \quad (11)$$

meaning that the oxygen atom, center-of-mass of the molecule, and center-of-mass of the two hydrogens lie on  $z$ -axis.

One could ask how do the changes in the hyperspherical coordinates  $R$ ,  $\phi$  and  $\theta$  manifest? We carried the change of the positions of the atoms connected with hyperspherical coordinates  $R$ ,  $\phi$  and  $\theta$  for  $\alpha$ - and  $\gamma$ -set along with normal coordinates (taken from [33]) in Fig. 4. We can identify oscillations in  $Q_1$  and  $R$  as symmetric stretching, in  $Q_2$  and  $\phi$  ( $\gamma$ -set) as bending and in  $Q_3$  and  $\phi$  ( $\alpha$ -set) as asymmetric stretching. Mode in hyper-angle  $\theta$  ( $\gamma$ -set) reflects the symmetry of the asymmetric bond-stretching in  $Q_3$  but does not seem to be a linear combination of the three normal modes as the position of the oxygen atom does not change. Let us note that the modes in  $Q_2$  and  $\phi$  ( $\gamma$ -set), although similar-looking, are not identical, and moreover, act in opposite directions: since for increasing  $Q_2$  the molecule straightens whereas

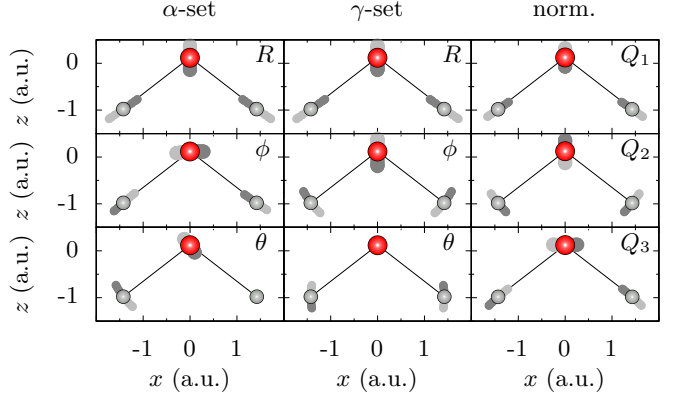


FIG. 4. Visualization of hyperspherical modes in  $\alpha$ - and  $\gamma$ -set, and normal modes, as change in the positions of individual atoms. Center-of-mass of the molecule is fixed at the origin and normal coordinates  $Q_1$ ,  $Q_2$  and  $Q_3$  and hyperspherical  $R$ ,  $\phi$  and  $\theta$  coordinates executes oscillation over one whole period. Positions of the atoms during the first half-period are carried out with light gray and for the second half-period with dark gray, respectively. The displacements of oxygen atom are exaggerated by a factor of 10. For more details see text.

for increasing  $\phi$  the molecule bends more. To conclude this comparison we note that the modes in  $Q_3$  and  $\phi$  ( $\alpha$ -set) are not identical either.

In addition, we have analyzed the atomic displacements in  $\gamma$ -set of hyperspherical coordinates analytically and the results are given in Appendix. A.

## II. ADIABATIC APPROXIMATION IN HYPERSPHERICAL COORDINATES

### A. The Born-Oppenheimer approximation

In order to simplify Eq. (5), we apply the well-known Born-Huang expansion of the wave function  $\psi(R, \phi, \theta)$  in the form

$$\psi(R, \phi, \theta) = \sum_{\nu} F_{\nu}(R) \Phi_{\nu}(R, \phi, \theta). \quad (12)$$

When we insert the expansion into Eq. (5) with the vibrational term from Eq. (8) and assume adiabatic behavior with respect to the  $R$  coordinate, we arrive at two coupled equations

$$\left( \frac{\Lambda^2 - 1/4}{2\mu R^2} + V(R, \phi, \theta) \right) \Phi_{\nu}(R, \phi, \theta) = U_{\nu}(R) \Phi_{\nu}(R, \phi, \theta), \quad (13)$$

$$\left( -\frac{1}{2\mu} \frac{d^2}{dR^2} + U_{\nu}(R) \right) F_{\nu n}(R) = E_{\nu n} F_{\nu n}(R), \quad (14)$$

where index  $\nu$  represents the vibrational quantum number of the 2D wave function  $\Phi_{\nu}(R, \phi, \theta)$  with energy  $U_{\nu}(R)$  on slice of the potential, i.e.,  $V(R = \text{const.}, \phi, \theta)$ .

Later we will address the fact that the energies of two distinct vibrational states can become degenerate and even cross with changing  $R$ . Index  $n$  stands for the vibrational quantum number of 1D wave function  $F_{\nu n}(R)$  on 1D potential curve given by  $U_{\nu}(R)$  with fixed value  $\nu$ . The energy  $E_{\nu n}$  then represents the total vibrational energy of the molecule under the adiabatic approximation applied on the nuclear coordinates. We can treat  $R$  as a parameter in the first equation and as a coordinate in the second equation. Let us stress that all non-adiabatic terms in the second equation are omitted so it is equivalent to Born-Oppenheimer approximation for the “slow” coordinate  $R$ . It is known that such approximation leads to determination of the lower bound on the energy levels [34]. However the upper bound is usually closer to the real result [35] and can be obtained by reintroduction of the non-adiabatic term

$$W_{\nu\nu}(R) = -\frac{1}{2\mu} \langle \Phi_{\nu}(R) | \frac{d^2}{dR^2} | \Phi_{\nu}(R) \rangle, \quad (15)$$

into the round bracket on LHS of Eq. (14) [34]. The bracket stands for integration over the hyperangles  $\phi$  and  $\theta$ .

Let us also note that the energies  $E_{\nu n}$  generally do not correspond to nuclear vibrational energies on the 3D adiabatic PES  $V(R, \phi, \theta)$ , unless the vibrational modes in  $R$  and  $(\phi, \theta)$  truly separate and all non-adiabatic corrections and couplings vanish, e.g., due to a proper choice of coordinate system. In such case, the energies  $E_{\nu n}$  would correspond to the full 3D nuclear vibrational energies in the sense of the Born-Oppenheimer approximation separating electronic and nuclear motion.

## B. Non-Adiabatic Coupling terms

Eqs. (13,14) are obtained by assuming that the non-adiabatic terms are negligible, thus leading to the conclusion that the various states  $F_{\nu n}(R)$  do not interact. If the non-adiabatic couplings are included, the full equation Eq. (14) would take the form:

$$\left( -\frac{1}{2\mu} \frac{d^2}{dR^2} + U_{\nu}(R) + W_{\nu\nu}(R) - E_{\nu} \right) F_{\nu}(R) = -\sum_{\rho \neq \nu} \left( W_{\nu\rho}(R) + 2V_{\nu\rho}(R) \frac{d}{dR} \right) F_{\rho}(R), \quad (16)$$

where

$$V_{\nu\rho}(R) = -\frac{1}{2\mu} \langle \Phi_{\nu}(R) | \frac{d}{dR} | \Phi_{\rho}(R) \rangle, \quad (17)$$

$$W_{\nu\rho}(R) = -\frac{1}{2\mu} \langle \Phi_{\nu}(R) | \frac{d^2}{dR^2} | \Phi_{\rho}(R) \rangle. \quad (18)$$

The Hamiltonian can be decomposed into two terms

$$H^{(1D)} = H_{\text{diag.}}^{(1D)} + H_{\text{coupl.}}^{(1D)}. \quad (19)$$

The diagonal Hamiltonian has the following form

$$H_{\text{diag.}}^{(1D)} = -\frac{1}{2\mu} \frac{d^2}{dR^2} + U_{\nu} + W_{\nu\nu}(R), \quad (20)$$

and the non-adiabatic couplings can be written as

$$H_{\text{coupl.}}^{(1D)} = \begin{pmatrix} 0 & W_{12}(R) + 2V_{12}(R) \frac{d}{dR} & \cdots \\ W_{21}(R) + 2V_{21}(R) \frac{d}{dR} & 0 & \ddots \\ \vdots & \ddots & \ddots \end{pmatrix}. \quad (21)$$

## C. Solving the 2D angular Schrödinger equation with 2D B-Splines

Eq. (13) can be solved trivially over some real 2D basis set. For this purpose we decided to use 2D B-Splines of some order  $k$ , chosen to be the same in both dimensions. Then, the wave function can be decomposed as

$$\Phi_{\nu}(R, \phi, \theta) = \sum_n c_{\nu n}(R) B_n(\phi, \theta), \quad (22)$$

where  $B_n(\phi, \theta)$  is the  $n$ -th 2D B-Spline and the coefficients  $c_{\nu n}(R)$  are R-dependent constants. The index  $n$  represents a unique product of two 1D B-Splines of order  $k$  constructed on grid of  $N_{\phi}$  points in one dimension and  $N_{\theta}$  points in the other (see, e.g., [36]). We have chosen  $k = 6$  and  $N_{\phi} = 46$  and  $N_{\theta} = 91$ .

In the B-Spline representation, Eq. (13) yields

$$\sum_n H_{n'n}^{(2D)}(R) c_{\nu n}(R) = \sum_n I_{n'n} c_{\nu n}(R), \quad (23)$$

with the Hamiltonian and overlap matrices as:

$$\begin{aligned} H_{n'n}^{(2D)} &= \langle B_{n'}(\phi, \theta) | \hat{H}_{2D} | B_n(\phi, \theta) \rangle, \\ I_{n'n} &= \langle B_{n'}(\phi, \theta) | B_n(\phi, \theta) \rangle. \end{aligned} \quad (24)$$

When we substitute for the grand angular momentum operator from Eq. (9) into Eq. (13), we can evaluate the matrix elements of the angular Hamiltonian as

$$\begin{aligned} H_{n'n}^{(2D)} &= \iint d\phi d\theta \sin \theta B_{n'}^* \left( V - \frac{1}{8\mu R^2} \right) B_n \\ &+ \frac{1}{2\mu R^2} \iint d\phi d\theta \sin \theta \left( \frac{\partial B_{n'}^*}{\partial \phi} \frac{\partial B_n}{\partial \phi} \right. \\ &\left. + \frac{1}{\sin^2 \phi \cos^2 \phi} \frac{\partial B_{n'}^*}{\partial \theta} \frac{\partial B_n}{\partial \theta} \right), \end{aligned} \quad (25)$$

where we applied the boundary conditions:  $\psi(R, 0, \theta) = \psi(R, \pi/2, \theta) = 0$  and  $\partial \psi / \partial \theta = 0$  at  $\theta = 0, \pi$ . The overlap matrix can be evaluated simply as

$$I_{n'n} = \iint d\phi d\theta \sin \theta B_{n'} B_n. \quad (26)$$

The diagonalization of this symmetric generalized eigenvalue problem can be done by standard packages (e.g., Lapack for Fortran). The energies  $U_{\nu}$  carried out for  $R = 1.88$  a.u. are presented in Tab. I. In this table, quantum numbers  $\nu_{\phi}$  and  $\nu_{\theta}$  are assigned from the nodal structure. Take  $U_1$  and  $U_3$  as the elementary quanta, it can be seen that the 2D eigenvalues are well approximated by  $E_{\nu_{\phi}, \nu_{\theta}} = \nu_{\phi} U_1 + \nu_{\theta} U_3$ .

$\nu$	$\nu_\phi$	$\nu_\theta$	$E_{\nu_\phi, \nu_\theta}$ (cm $^{-1}$ )	$U_\nu$ (cm $^{-1}$ )	rel. diff. (%)
0	0	0	0	0	-
1	1	0	1634.3	1634.3	-
2	2	0	3268.7	3238.2	0.9
3	0	1	4111.9	4111.9	-
4	3	0	4903.0	4803.7	2.1
5	1	1	5746.3	5770.1	0.4
6	4	0	6537.4	6320.3	3.4
7	2	1	7380.6	7397.6	0.2
8	5	0	8171.7	7770.9	5.2
9	0	2	8223.8	8368.9	1.7
10	3	1	9014.9	8986.8	0.3
11	6	0	9806.1	9122.8	7.5
12	1	2	9858.2	10050.8	1.9
13	7	0	11440.4	10343.4	9.6
14	4	1	10649.3	10527.6	1.1
15	8	0	13074.8	11537.5	13.3
16	2	2	11492.5	11701.7	1.8
17	5	1	12283.6	12003.9	2.3
18	0	3	12335.7	12763.8	3.4
19	9	0	14709.1	12874.7	14.2
20	3	2	13126.9	13314.4	1.4

TABLE I. Analysis of the separation of the potential at  $R = 1.88$ . We compare the quantized energies constructed via  $E_{\nu_\phi, \nu_\theta} = \nu_\phi U_1 + \nu_\theta U_3$  with the calculated energies  $U_\nu$  of 2D Eq. (13). The overall small relative difference indicates that the potential behaves like separable in the two hyperangles.

### III. SEMI-SEPARABILITY OF THE POTENTIAL IN HYPERSPHERICAL COORDINATES

Normal vibration modes of the water molecule are based on the strict assumption that the potential is sep-

arable in the normal coordinates, for example, at least at the equilibrium position, and that vibrational states are independent and quantized with unique quantum numbers and unique energies. As we will discuss further, this is not true for highly excited states. Nevertheless, such simple picture is not far from reality and this picture helps us to gain insight into the behavior of molecular dynamics.

We have already separated the potential into hyperradial and hyperangular parts in our adiabatic approach, can the equivalent of the three normal modes occur also in hyperspherical approach?

The answer is not obvious since the grand angular momentum operator  $\Lambda^2$  from Eq. (9) is not separable in the hyperangles. Nevertheless, we can use a small trick if we assume separability of the 2D wave function with parameter  $R$  and the quantum numbers  $\nu_\phi$  and  $\nu_\theta$  in the form

$$\tilde{\Phi}_{\nu_\phi, \nu_\theta}(R, \phi, \theta) = \Phi_{\nu_\phi}(R, \phi)\Theta_{\nu_\theta}(R, \theta). \quad (27)$$

Such a separable form would yield the approximate total 2D energy as

$$\tilde{U}_{\nu_\phi, \nu_\theta} = U_{\nu_\phi} + U_{\nu_\theta}. \quad (28)$$

This trick comes handy when separation of the grand angular momentum operator along with the molecular potential  $V(R, \phi, \theta)$  at the minimum of the potential  $(\phi_{\min}, \theta_{\min})$  for a given  $R$  is set by

$$\begin{aligned} \left( \frac{\Lambda_\phi^2 - 1/8}{2\mu R^2} + V(R, \phi, \theta_{\min}) - \frac{1}{2}V(R, \phi_{\min}, \theta_{\min}) \right) \Phi_{\nu_\phi}(R, \phi) &= U_{\nu_\phi} \Phi_{\nu_\phi}(R, \phi), \\ \left( \frac{\Lambda_\theta^2 - 1/8}{2\mu R^2} + V(R, \phi_{\min}, \theta) - \frac{1}{2}V(R, \phi_{\min}, \theta_{\min}) \right) \Theta_{\nu_\theta}(R, \theta) &= U_{\nu_\theta} \Theta_{\nu_\theta}(R, \theta), \end{aligned} \quad (29)$$

where the separated grand angular operators yield

$$\begin{aligned} \Lambda_\phi^2 &= -\frac{\partial^2}{\partial \phi^2}, \\ \Lambda_\theta^2 &= -\frac{1}{\sin^2 \phi_{\min} \cos^2 \phi_{\min} \sin \theta} \frac{\partial}{\partial \theta} \left( \sin \theta \frac{\partial}{\partial \theta} \right). \end{aligned} \quad (30)$$

Let us note that the quantities obtained within separability approximation will be marked with a tilde.

Although this separation may seem arbitrary, it is well founded by the quantization of the 2D wave functions

$\Phi_\nu(R, \phi, \theta)$  in the quantum numbers  $\nu_\phi$  and  $\nu_\theta$  as we can see in Tab. I.

This also explains why the resulting potential energy curves (PEC)  $\tilde{U}_{\nu_\phi, \nu_\theta}$  are very close to the curves obtained by full 2D calculations (calculated with B-Spline basis set), see Fig. 5 (a) and (b)). Not only the order of the curves in  $U_\nu^{(2D)}$  and  $\tilde{U}_{\nu_\phi, \nu_\theta}$  are identical, but also the positions of all curve crossings. Exact numerical values at  $R = 1.88$  for these two calculations can be found in Tab. II.

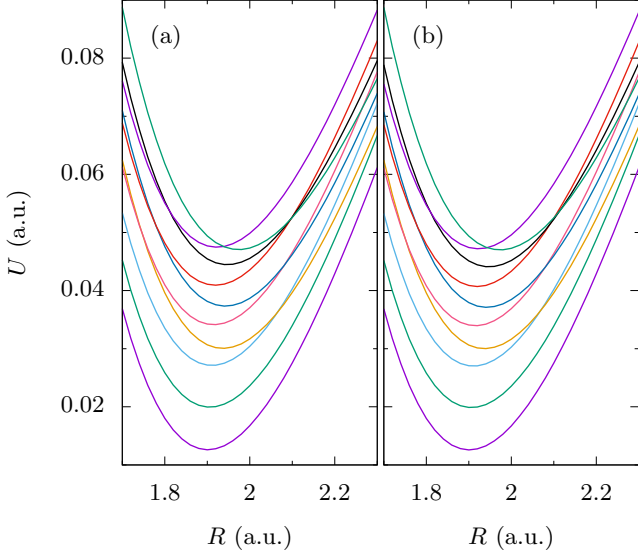


FIG. 5. Adiabatic PEC  $U_\nu^{(2D)}$  obtained by solving Eq. (13) with 2D B-Spline basis set are shown in panel (a) and  $\tilde{U}_{\nu_\phi, \nu_\theta}$  obtained by separable approximation are plotted in panel (b).

$\nu$	$\nu_\phi$	$\nu_\theta$	$\tilde{U}_{\nu_\phi, \nu_\theta}$	$\tilde{H}_{(\nu)}^{(\text{full})}$	$\tilde{E}_{(\nu)}^{(\text{full})}$	$U_\nu^{(2D)}$
0	0	0	0.01280	0.01287	0.01283	0.01283
1	1	0	0.02020	0.02047	0.02027	0.02027
2	2	0	0.02746	0.02808	0.02758	0.02758
3	0	1	0.03152	0.03174	0.03156	0.03156
4	3	0	0.03455	0.03578	0.03472	0.03472
5	1	1	0.03892	0.03977	0.03912	0.03912
6	4	0	0.04142	0.04384	0.04163	0.04163
7	2	1	0.04618	0.04813	0.04653	0.04653
8	5	0	0.04801	0.05322	0.04830	0.04823
9	0	2	0.05093	0.05130	0.05096	0.05096

TABLE II. Comparison of energies at  $R = 1.88$  a.u. for low lying states obtained by several methods as discussed in text. Energies  $\tilde{U}_{\nu_\phi, \nu_\theta}$  are determined under the assumption of separable potential while  $U_\nu^{(2D)}$  are true adiabatic potential. Diagonal full Hamiltonian matrix elements  $\tilde{H}_{(\nu)}^{(\text{full})}$  gives the energy of the 2D Hamiltonian if the eigenstates are separable.  $\tilde{E}_{(\nu)}^{(\text{full})}$  gives the energy after diagonalization of 2D Hamiltonian with basis constructed by the separable states. Thus the separable states can serve as a diabatic basis set.

### A. Reconstructing $\tilde{\Phi}(\phi, \theta)$

The huge advantage of having two 1D Schrödinger equations instead of one 2D equation is the speed of calculation. The other great advantage is the trivial organization of the eigenstates. The 1D eigenstates in each dimension are quantized with corresponding quantum number  $\nu_\phi$  or  $\nu_\theta$ . Energies of these 1D states increase monotonically with the increasing quantum number and similar states in various  $R$ -slices of the PES can be easily assigned. Such organization also applies for the constructed 2D wave functions  $\tilde{\Phi}_{\nu_\phi, \nu_\theta}$ . This is not

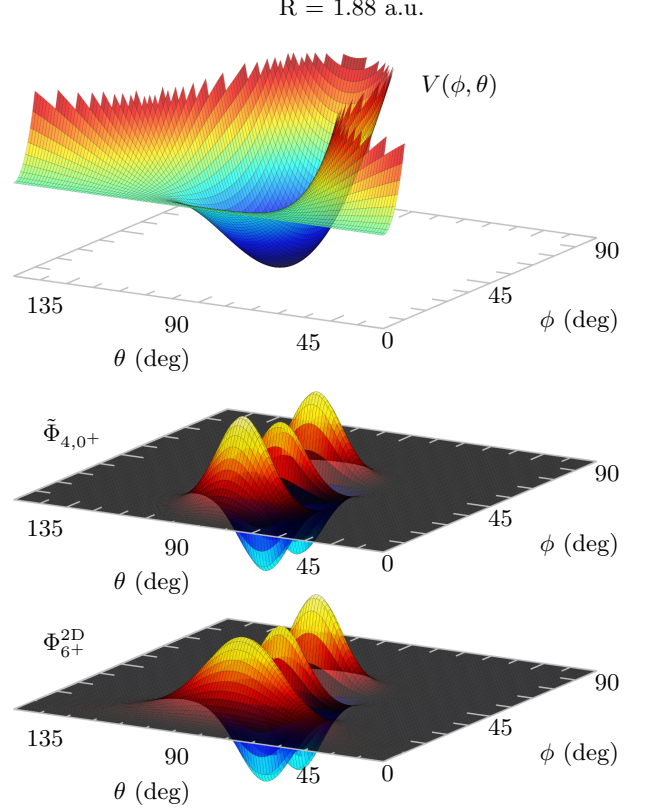


FIG. 6. (Top panel) A slice of potential  $V(R = 1.88, \phi, \theta)$ . Comparison of the 2D adiabatic wave function (bottom panel) for the 7th state ( $\nu = 6$ ) in Table II with the separable wave function (middle panel) for  $\tilde{\Phi}_{4,0+}$ . The superscript + indicates the symmetry in hyperspherical coordinate  $\theta$ .

true for the adiabatic 2D states as there are slices, where quasi-separability breaks down and nodes in the two dimensions cannot be distinguished. Trying to connect the 2D adiabatic states in neighboring slices via their overlap,  $\langle \Phi_\nu(R_i) | \Phi_{\nu'}(R_{i+1}) \rangle$ , works for the four lowest lying states only, while for higher lying states they cannot be connected correctly via this method through split of the potential at  $R \approx 2.43$ . Further challenge is posed at  $R \approx 3.19$  a.u. where the full 2D eigenfunctions also lack clear nodal structure in each dimension making the connection rather nontrivial.

The natural thing to ask is how precise are the 2D wave functions constructed by two 1D wave functions obtained from the separation method in Eq. (29)? To answer this question we can use two ways. On one hand, we can evaluate the overlap between the constructed states and the real 2D states

$$a_{i,(\nu)} = \langle \Phi_i | \tilde{\Phi}_{(\nu)} \rangle \quad (31)$$

where hyperindex  $(\nu)$  represents one particular combination of quantum numbers  $\nu_\phi, \nu_\theta$ . The assignment of  $\nu_\phi, \nu_\theta$  to the hyperindex  $\nu$  follows the scheme from Tab. II (for

$i = \backslash (\nu) =$	(0)	(1)	(2)	(3)	(4)	(5)	(6)	(7)	(8)	(9)
0	0.999	0.025	0	0	0.001	0	0	0	0	0.007
1	0.026	0.997	0.032	0	0.002	0	0.003	0	0.001	0.034
2	0.001	0.038	0.993	0	0.035	0	0.005	0	0.006	0.012
3	0	0	0	0.996	0	0.075	0	0.003	0	0
4	0	0.002	0.049	0	0.987	0	0.033	0	0.012	0.004
5	0	0	0	0.079	0	0.985	0	0.098	0	0
6	0	0	0.004	0	0.060	0	0.976	0	0.025	0.001
7	0	0	0	0	0	0.115	0	0.970	0	0
8	0	0	0.001	0	0.007	0	0.073	0	0.959	0
9	0.010	0.037	0.020	0	0	0	0	0	0	0.989

TABLE III. Projections  $a_{i,(\nu)}$  at  $R = 1.88$  a.u. Here the row number indicates the level order of the adiabatic state, the column number is the order  $\nu$  of the separable state (corresponding to the first column in Table II). The off-diagonal terms indicate the degree of coupling.

example, if  $\nu = 6$  then  $\nu_\phi = 4$  and  $\nu_\theta = 0$ ). We show the projections in Tab. III. On the other hand, we can evaluate the full Hamiltonian matrix

$$\tilde{H}_{(\nu_1)(\nu_2)}^{(\text{full})} = \left\langle \tilde{\Phi}_{(\nu_1)} \left| \frac{\Lambda^2 - 1/4}{2\mu R^2} + V \right| \tilde{\Phi}_{(\nu_2)} \right\rangle, \quad (32)$$

with hyperindices  $(\nu_1)$  and  $(\nu_2)$ . The more the diagonal elements of the matrix  $\tilde{H}_{(\nu)(\nu)}^{(\text{full})}$  deviate from the corresponding energy  $\tilde{U}_{\nu_\phi, \nu_\theta}$ , the more the constructed wave functions deviate from the true adiabatic 2D wave functions. Such deviations start to become prominent for the 7th ( $\nu = 6$ ) and 9th ( $\nu = 8$ ) levels. The discrepancy can be attributed to the high quantum number  $\nu_\phi$  (4 and 5, respectively) which is connected to a wider spread of the wave function in the  $\phi$ -direction, where the full shape of the potential starts to play a role. As we can see in Fig. 6 where we compare the 2D slice of  $V(R = 1.88, \phi, \theta)$ , the constructed  $\tilde{\Phi}_{(6)}$  with the true 2D  $\Phi_6$ . The wave function 2D  $\Phi_6$  differs from  $\tilde{\Phi}_{(6)}$  mainly in the first lobe which is somewhat broader and lower, which can be attributed trivially to “opening” of the potential at small values of  $\phi$ . Nevertheless, this difference, although having rather small influence on the energy of the state (see Tab. III), does cause a non-negligible mixing with other states, as evidenced by the significant deviation of  $\tilde{H}_{(6)(6)}^{(\text{full})}$  from  $\tilde{U}_{4,0}$ . We also diagonalized the full Hamiltonian matrix evaluated over a basis of 400 states  $\tilde{\Phi}_{\nu_\phi, \nu_\theta}$  with  $\nu_\phi, \nu_\theta = 1, \dots, 20$  and carried out the ten lowest eigenenergies  $\tilde{E}_{(\nu)}^{(\text{full})}$  in Tab. II. The correspondence between the eigenenergies and the real adiabatic 2D values indicates that the constructed states can be used a diabatic basis set.

Once the 2D basis functions  $\tilde{\Phi}_{\nu_\phi, \nu_\theta}$  are constructed for the range of  $R$  of interest, we can trivially carry out the corresponding 1D  $\tilde{U}_{\nu_\phi, \nu_\theta}(R)$ . In particular, as shown in Fig. 7, the potential curves can be labelled as symmetric or antisymmetric in accordance with the even or odd quantum numbers  $\nu_\theta$  and with respect to the symmetry in hyperangle  $\theta$ .

## B. Split of potential in $\theta$ and appearance of saddle

The OH + H dissociation limit along with the symmetry of the molecule leads to formation of a barrier at a particular size (or  $R$ ) of the molecule when it begins to be energetically favorable for one of the hydrogen atoms to shift farther away from oxygen than the other. This twofold dissociation limit manifests trivially only in the  $\gamma$ -set as the split of the potential minimum appears only in the hyperangle  $\theta$ . The barrier arises at the hyperradius  $R \approx 2.4$  as shown in Fig. 3.

The PES in  $\gamma$ -set manifests symmetry in the hyperspherical angle  $\theta$  which is also preserved by the 1D wave functions  $\Theta_{\nu_\theta}$  and 1D potential  $V(\theta) = V(R, \phi_{\min}, \theta) - V(R, \phi_{\min}, \theta_{\min})$ . Therefore we can restrict our initial analysis to one dimension only. The formation of the barrier in the hyperangle  $\theta$  is visualized in Fig. 8.

With increasing  $R$  the value of the minimum of the potential increases and a barrier at  $\theta = 90^\circ$  starts to form. Moreover, the height of the barrier grows with the increasing hyperradius. As the height of the barrier increases, the energy difference between the neighboring states of opposite symmetry decreases till the states become degenerate at some point. The energies of lower lying states converge to each other faster than the energies of higher lying states which is trivially understandable as a creation of two separate potential wells affects lowest states mostly. We should note that only the states with opposite symmetry merge together. The rising of the potential barrier will affect the antisymmetric states less since they have a node at  $\theta = 90^\circ$ . For the symmetric states, as the potential barrier rises, the wave functions at and near  $\theta = 90^\circ$  are in the classical forbidden region, thus with nonzero but very small probabilities. Therefore, the energy of the symmetric states will become very close to antisymmetric states since in both cases the wave functions in the barrier regions are both very small, resulting in the pair of symmetric and antisymmetric curves merging at large  $R$  where the potential barrier is high.

Now, we can understand why the two neighboring PECs of opposite symmetry merge together while staying separated from other PEC pairs of the same  $\nu_\phi$  in

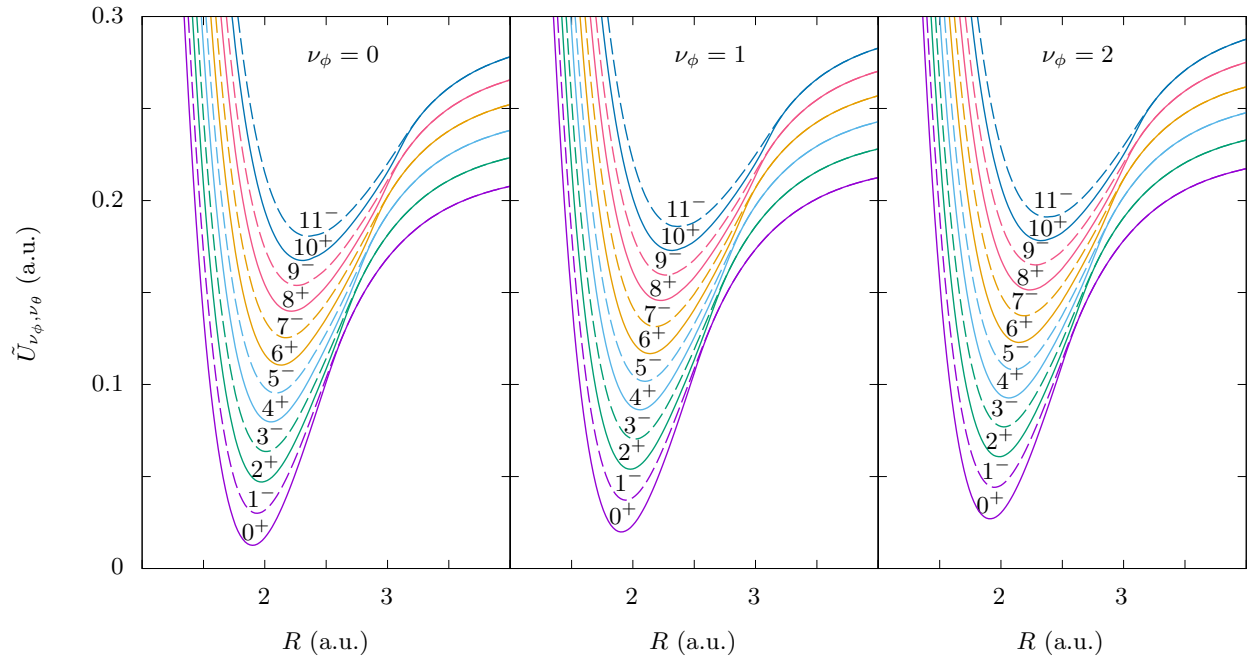


FIG. 7. Depiction of several lowest energies  $\tilde{U}_{\nu_\phi=0,1,2;\nu_\theta}$  of the 2D states  $\tilde{\Phi}_{\nu_\phi,\nu_\theta}$  constructed via the separation method. The PEC of the same  $\nu_\phi$  are separable without any crossings. The states symmetric in  $\theta$  are shown by full lines and marked with superscript +, the antisymmetric states by dashed lines and superscript -. The potential energy curves for states with opposite symmetry and  $\nu_\theta = 2n - 2$  and  $\nu_\theta = 2n - 1$  are shown with the same color. Each pair merges into a single curve at large  $R$ . As expected, the merging occurs at larger values of  $R$  with increasing quantum number  $\nu_\theta$ .

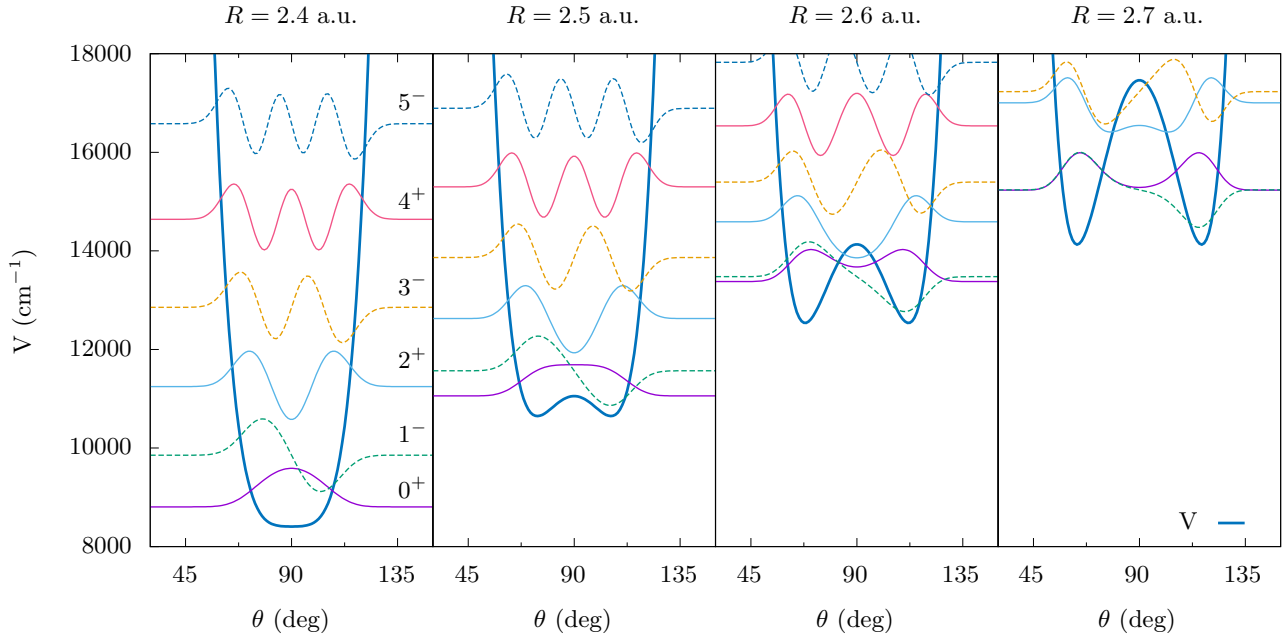


FIG. 8. Formation of the barrier in the molecular potential visualized as 1D slice. The potential  $V(\theta) = V(R, \phi_{min}, \theta) - \frac{1}{2}V(R, \phi_{min}, \theta_{min})$  is shown in a thick blue line while low-lying states  $\Theta_{\nu_\theta}$  are shown in thin colored lines. With increasing hyperradius  $R$ , a single potential well at small  $R$  will deform into two potential wells, separated by a growing potential barrier. As the barrier grows, the wave function of the symmetric state in the barrier region become very small, thus its energy becomes very close to the antisymmetric state, resulting in pairs of degenerate states at large hyperradius. Note that nodal structure of the wave functions do not change versus  $R$ .

Fig. 7 and what role is played by the barrier. In top row of Fig. 9 we demonstrate how the barrier emerges in 2D.

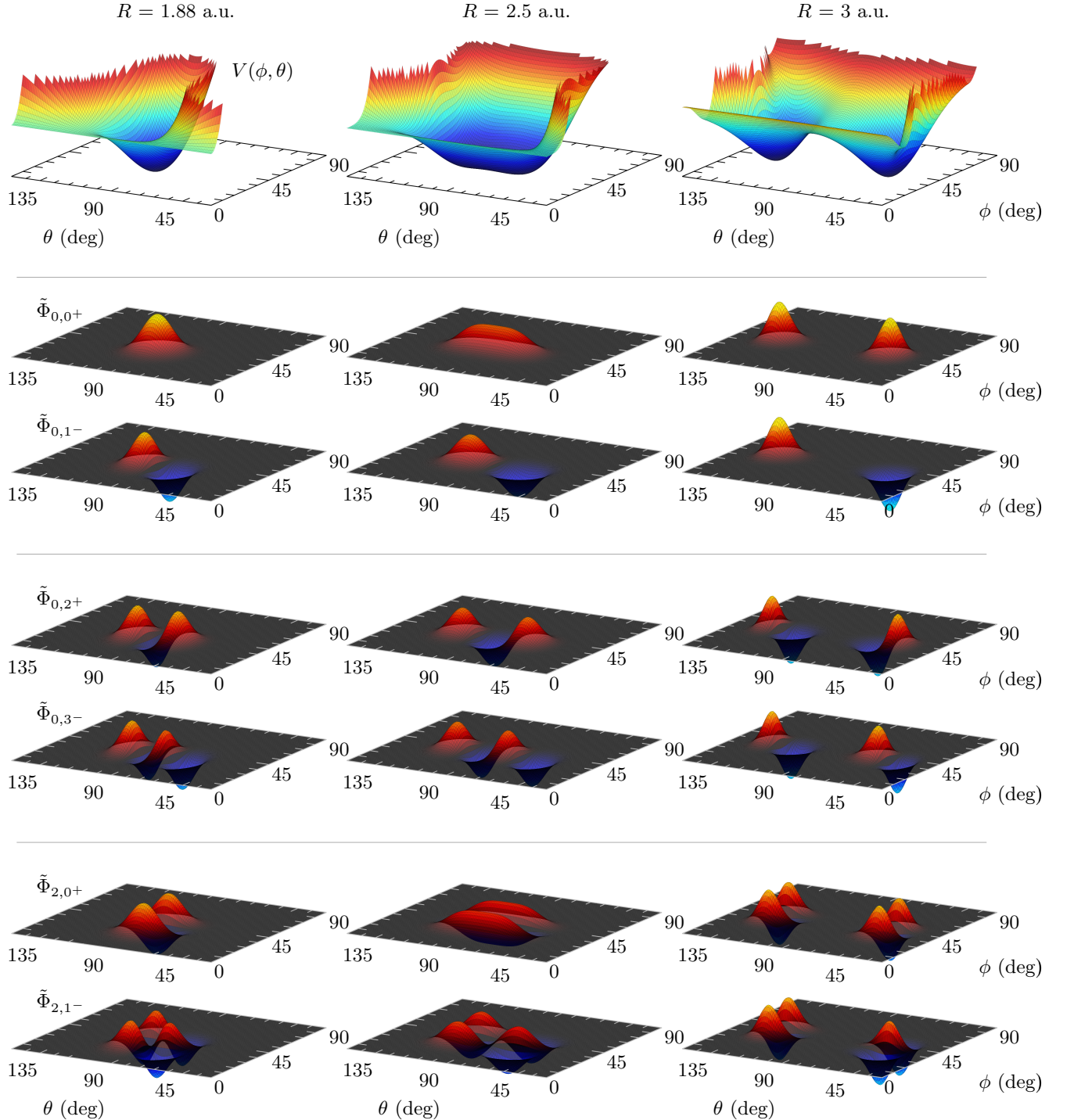


FIG. 9. We plotted three most distinct shapes of the PES slices with respect to value of  $R$  on the first line. As we can see the 2D PES slices evolve from having one minimum ( $R \lesssim 2.4$  a.u.) towards having two distinct minima ( $R \gtrsim 2.4$  a.u.) separated by a saddle-like barrier with height increasing with  $R$ . On the remaining lines we carried out the corresponding 2D functions  $\tilde{\Phi}_{\nu_\phi, \nu_\theta}$  which we organized with respect to their symmetries in  $\theta$  and energy degeneracy at large  $R$ . The deformation of the symmetric states due to the barrier is more severe than of the antisymmetric states leading to creation of degenerate energy pairs as we already discussed for the 1D slices in text.

At equilibrium  $R = 1.88$ , as seen in the first potential surface in the top row, there is only one minimum in  $\theta$ .

Near  $R = 2.5$ , this minimum begins to split, where a saddle starts to form, and the two minima shift apart with

increasing  $R$ , as shown for  $R = 3$  (see Fig. 3(c)-(d) for more details on the position of the minima). In the remaining rows of Fig. 9, we show how the 2D  $\tilde{\Phi}_{\nu_\phi, \nu_\theta}(\phi, \theta)$  wave functions evolve with  $R$  for three pairs of states where each pair becomes degenerate at large  $R$ . Before the saddle, the symmetric state lies much lower than the antisymmetric state, where the symmetric state has much larger probability distributions near the symmetry point  $\theta = 90^\circ$ . At the saddle, each wave function begins to spread and eventually the wave function splits into two distinct parts at  $R = 3$ . In doing so, the nodal structure at  $\theta = 90^\circ$  remains the same. Since the barrier height increases with  $R$ , the large probability density for the symmetric state at  $\theta = 90^\circ$  begins to diminish. For large  $R$ , the probability density for symmetric and antisymmetric states in the barrier region both become very small, leading to two degenerate states at large  $R$  in each pair. Such “bifurcation” at the saddle occurs at increasing  $R$  as the vibrational energies of the states increase. For such degenerate states, linear combination of the symmetric and antisymmetric states would result in two localized states,

$$\begin{aligned}\tilde{\Phi}_{\text{H+OH}} &= \frac{\tilde{\Phi}_{0,0+} + \tilde{\Phi}_{0,1-}}{\sqrt{2}}, \\ \tilde{\Phi}_{\text{HO+H}} &= \frac{\tilde{\Phi}_{0,0+} - \tilde{\Phi}_{0,1-}}{\sqrt{2}}.\end{aligned}\quad (33)$$

These two localized states would be related to either case of the attachment of one hydrogen atom to oxygen atom with the other hydrogen atom far away. Fig. 10 illustrates such cases at  $R = 4$  a.u. On top frames, we illustrate the 2D potential surface, highlighting where the potential wells are located in each set of Jacobi coordinates and the exact positions of the minima are marked by white crosses. For each localized state, the wave function is confined only to one narrow region, as clearly seen in each Jacobi set of hyperspherical angles illustrated on middle and bottom frames.

Each linear combination represents the dissociation limit for different hydrogen atom as indicated by the subscript. Such localization of the hyperspherical modes towards dissociation of one or the other hydrogen atom is possible only due to the energy degeneracy for symmetric and antisymmetric neighboring states. We should keep in mind that the degeneracy of the two neighboring states appears at a particular value of  $R$  which depends on their energy via quantum numbers  $\nu_\phi$  and  $\nu_\theta$  as discussed in Fig. 7.

Let us remark that the creation of energy-degenerate pairs at large hyperradii was also observed for the true 2D wave functions and is well reproduced in the present approach.

So far, we have developed a framework adiabatically connecting equilibrium vibration states with dissociative vibrational states at large hyperradii. Intuitively, the most efficient control of dissociative products by ultrafast pulses is to manipulate these states in the transition region. Such knowledge would be invaluable for optimization of reaction products in the future.

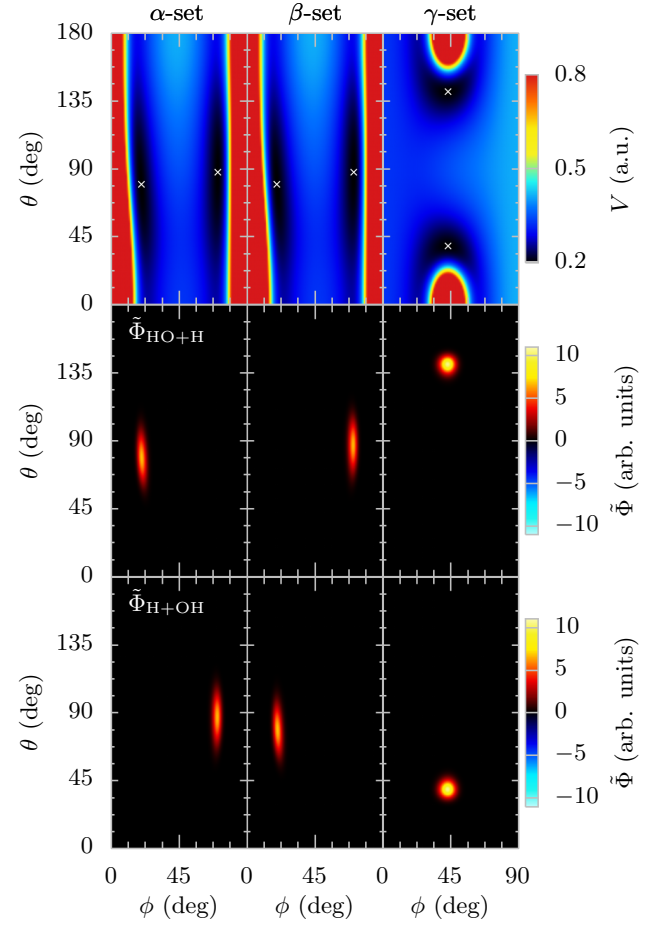


FIG. 10. Top row: 2D potential slice  $V(\phi, \theta)$  at  $R = 4$  a.u. for the three sets of hyperspherical coordinates. The dark blue regions indicate the potential wells with minima marked by white crosses separated by the saddle which looks differently in each set. Middle and bottom row: the localized wave functions given in Eq. (33). As we can see, each wave function is represented by a well localized state, corresponding to the dissociation of a different hydrogen atom via corresponding potential minimum.

#### IV. CONSTRUCTION OF THE FULL VIBRATIONAL STATES

The full vibrational states can now be constructed via Eq. (14) using PEC from Eq. (28). The correct procedure should involve also the non-adiabatic corrections as shown in Eq. (16), but since our PEC was already evaluated in the separable approximation of the potential, it makes little sense to incorporate the relatively small non-adiabatic terms to increase the precision. Nevertheless, it is worth noting that the non-adiabatic correction terms peak at the split of the potential at  $R \approx 2.4$  a.u. which is the place where the symmetric and antisymmetric states start to degenerate in energy.

For illustration we carried out the four lowest 1D solutions  $F_{\nu_R}(R)$  on the lowest PEC  $\tilde{U}_{\nu_\phi=0, \nu_\theta=0+}(R)$  in

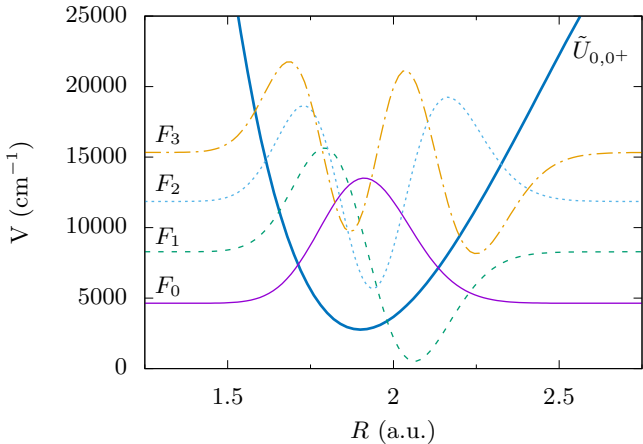


FIG. 11. The four lowest 1D solutions  $F_n(R)$  to the Eq. (14) with  $\tilde{U}_{0,0+}(R)$ .

Fig. 11. One could ask how precise are the energies  $E_{\nu_R, \nu_\phi, \nu_\theta}$  after all these approximations are made. Interestingly, the computed energies are very precise for energies up to roughly  $19\ 500\ \text{cm}^{-1}$ . In this comparison, the data were obtained with optimized Discrete Variable Representation calculated with other type of hyperspherical coordinates but on the same PES in [30]. The zero-point-energy we determined is  $4635.14\ \text{cm}^{-1}$ , as compared to the value of  $4629.98\ \text{cm}^{-1}$  given in Neto and Costa in [30], a difference of only  $5.2\ \text{cm}^{-1}$ .

Nevertheless, it is expected that the zero-point-energy will be reproduced correctly as the ground state lies in the separability region and the non-adiabatic corrections are the smallest. As we have already mentioned, the approximation of separability introduces discrepancies for highly excited 2D states (e.g.,  $\Phi_{4,0+}$ ) and therefore errors are expected to rise with increasing quantum state. To get a better picture of the errors introduced with the approximations we show a list of low-lying vibrational states labelled by the three quantum numbers which are readily available based on the separable approximations. The vibrational energy levels obtained from the present calculations are then compared to those given by Neto and Costa [30] in Tab. IV. The relative error of the calculated energies at most are about 2-3%, but mostly are under one percent.

As the largest source of discrepancy between the result presented here and [30], we regard the breakdown of the potential semi-separability from Eqs. (29) in the two hyperangles for higher excitation states. We also found that inclusion of the diagonal non-adiabatic terms  $W_{\nu\nu}(R)$  does not generally improve the results in Tab. IV.

## V. DISCUSSIONS

In this report we have addressed the separability of nuclear vibrational states in a water molecule in its elec-

tronic ground state in hyperspherical coordinates as an alternative to the well-known and somewhat complementary normal-mode and local-mode approaches. As the starting point, we applied adiabatic approximation in the hyperradius separating it from the two hyperangles. Further simplification of the problem was motivated by the observed semi-separability in the 2D energy spectra and verified in the separation of the 2D problem into two independent 1D problems for each hyperangle. The presented framework was then used for the construction of adiabatic 1D PECs as functions of the hyperradius. Classification and separability of all adiabatic 1D PECs with respect to the underlying quantum numbers associated with the hyperangles was discussed. Pair-wise degeneracy of two neighboring PECs of opposite symmetry at large values of hyperradius was observed and connected to formation of a saddle-like barrier associated with the twofold  $\text{OH} + \text{H}$  dissociation limit. The role of the barrier on the 2D vibrational states was thoroughly investigated and shape deformation followed by separation of symmetric states with increasing hyperradius was observed while the shape of antisymmetric states after separation remained unchanged. This not only explains the pair-wise degeneracy of 1D PECs but also provides a possibility to control the dissociation process as which of the two hydrogen atoms will dissociate from the molecule will be determined by the linear combination of the paired 2D wave functions. Possible control scheme emerges as these states are adiabatically linked to specific vibrational states near equilibrium geometry.

Finally, we have tested the validity of our framework by constructing the full 3D vibrational states within the adiabatic and separability approximation. The resulting energies yield an amazing correspondence to the high precision 3D calculations and differ maximally by 2.9% for the values up to  $19\ 500\ \text{cm}^{-1}$ .

Among the undeniable advantages of the presented framework we count the simplicity of vibrational state construction reducing the generally non-trivial 3D problem into three trivial 1D problems while yielding reasonably precise energies with only small deviations from the exact values. Let us note that the assignment and interpretation of vibrational quantum numbers in a full numerical 3D calculation can be very challenging especially when an unsuitable coordinate system was used. Nevertheless, the construction procedure presented here gives rise naturally to the vibrational quantum numbers which are easily understandable in the context of the separated hyperspherical modes.

It is also fair to mention that the present approach is not aimed at high precision calculation of vibrational energy levels. Whether approximate separability demonstrated here for water molecule can be extended to other molecular systems remains to be studied further. It is interesting to note that at least the separable vibrational wave functions constructed in this paper would serve as convenient diabatic basis functions for scattering calculations, thus replacing the complicated nonadiabatic

$\nu_R$	$\nu_\phi$	$\nu_\theta$	$E^{(\text{Neto})}$ (cm $^{-1}$ )	$E^{(\text{pres.})}$ (cm $^{-1}$ )	rel. diff. (%)	$\nu_R$	$\nu_\phi$	$\nu_\theta$	$E^{(\text{Neto})}$ (cm $^{-1}$ )	$E^{(\text{pres.})}$ (cm $^{-1}$ )	rel. diff. (%)	$\nu_R$	$\nu_\phi$	$\nu_\theta$	$E^{(\text{Neto})}$ (cm $^{-1}$ )	$E^{(\text{pres.})}$ (cm $^{-1}$ )	rel. diff. (%)
0	0	0	0	5.2	0.1	2	1	1	12155.6	12152.9	0.0	0	1	4	16056.5	16051.6	0.0
0	1	0	1594.2	1588.6	0.4	1	6	0	12341.5	12337.8	0.0	0	9	1	16109.4	16182.3	0.5
0	2	0	3151.7	3139.0	0.4	1	1	2	12407.5	12284.5	1.0	0	6	2	16186.4	15952.3	<b>1.5</b>
1	0	0	3656.1	3654.9	0.0	0	9	0	12504.5	12708.7	<b>1.6</b>	3	4	0	16524.3	16453.4	0.4
0	0	1	3755.6	3773.6	0.5	0	6	1	12566.5	12449.9	0.9	2	4	1	16540.1	16387.0	0.9
0	3	0	4667.3	4650.7	0.4	0	1	3	12570.5	12551.0	0.2	0	12	0	16670.8	17031.4	<b>2.1</b>
1	1	0	5233.8	5207.7	0.5	2	4	0	13194.9	13090.1	0.8	1	4	2	16783.2	16506.9	<b>1.7</b>
0	1	1	5331.6	5318.5	0.2	1	4	1	13251.7	13110.3	1.1	3	2	1	16822.8	16849.8	0.2
0	4	0	6133.7	6115.7	0.3	0	4	2	13452.8	13296.9	1.2	2	2	2	16825.1	16914.8	0.5
1	2	0	6774.5	6727.6	0.7	1	7	0	13605.4	13610.5	0.0	3	0	2	16898.8	17225.7	<b>1.9</b>
0	2	1	6872.9	6832.6	0.6	3	2	0	13646.8	13654.5	0.1	2	0	3	16898.6	17398.6	<b>2.9</b>
2	0	0	7202.1	7221.1	0.3	2	2	1	13657.7	13602.3	0.4	0	4	3	16973.6	16767.3	1.2
1	0	1	7250.3	7267.8	0.2	0	10	0	13796.7	14084.6	<b>2.0</b>	2	7	0	17055.7	16992.3	0.4
0	0	2	7444.4	7467.5	0.3	0	7	1	13798.7	13707.4	0.7	1	7	1	17157.0	16996.9	0.9
0	5	0	7539.4	7523.7	0.2	2	0	2	13828.7	14067.0	<b>1.7</b>	4	2	0	17224.9	16988.9	1.4
1	3	0	8272.6	8208.8	0.8	3	0	1	13831.0	13983.9	1.1	1	10	0	17316.5	17515.0	1.1
0	3	1	8375.0	8310.7	0.8	1	2	2	13910.7	13727.5	1.3	1	2	3	17319.1	17123.0	1.1
2	1	0	8762.2	8743.6	0.2	0	2	3	14075.0	13989.4	0.6	0	10	1	17378.6	17493.1	0.7
1	1	1	8808.9	8780.1	0.3	4	0	0	14222.4	14092.4	0.9	0	7	2	17434.5	17189.0	1.4
0	6	0	8862.8	8863.8	0.0	1	0	3	14320.5	14288.6	0.2	5	0	0	17460.0	17386.9	0.4
0	1	2	9001.4	8973.1	0.3	0	0	4	14540.4	14627.0	0.6	4	0	1	17495.9	17192.9	<b>1.8</b>
1	4	0	9719.1	9643.6	0.8	2	5	0	14548.3	14439.7	0.8	0	2	4	17541.3	17450.9	0.5
0	4	1	9832.0	9746.0	0.9	1	5	1	14629.4	14461.2	1.2	1	0	4	17753.6	17693.6	0.3
0	7	0	10073.4	10142.5	0.7	1	8	0	14778.4	14877.9	0.7	3	5	0	17876.8	17775.4	0.6
2	2	0	10284.9	10233.5	0.5	0	5	2	14858.3	14653.3	1.4	2	5	1	17902.1	17706.6	1.1
1	2	1	10331.6	10261.8	0.7	0	8	1	14932.6	14933.0	0.0	1	5	2	18120.0	17829.3	<b>1.6</b>
0	2	2	10524.8	10449.8	0.7	3	3	0	15108.6	15076.8	0.2	0	13	0	18194.7	18574.6	<b>2.0</b>
3	0	0	10601.9	10701.4	0.9	2	3	1	15121.5	15016.0	0.7	2	8	0	18260.0	18251.8	0.0
2	0	1	10614.8	10673.0	0.5	0	11	0	15190.2	15530.1	<b>2.2</b>	2	3	2	18273.1	18291.3	0.1
1	0	2	10868.5	10812.9	0.5	2	1	2	15349.1	15505.1	1.0	1	11	0	18695.7	18920.5	1.2
0	0	3	11033.3	11085.5	0.5	3	1	1	15354.2	15431.9	0.5	5	1	0	18957.7	18826.0	0.7
1	5	0	11081.7	11021.8	0.5	1	3	2	15376.0	15137.0	<b>1.6</b>	0	3	4	18994.9	18820.9	0.9
0	8	0	11234.4	11404.5	<b>1.5</b>	0	3	3	15544.2	15396.6	1.0	3	6	0	19147.8	19044.6	0.5
0	5	1	11234.6	11129.3	0.9	4	1	0	15742.9	15556.6	1.2	1	1	4	19249.7	19083.1	0.9
2	3	0	11765.3	11684.9	0.7	2	6	0	15809.5	15732.3	0.5	1	6	2	19377.1	19096.0	<b>1.5</b>
1	3	1	11814.6	11707.5	0.9	1	1	3	15838.0	15719.2	0.8	2	9	0	19493.2	19530.8	0.2
0	3	2	12010.7	11893.1	1.0	1	6	1	15922.4	15753.0	1.1	2	4	2	19664.8	19628.5	0.2
3	1	0	12143.5	12194.2	0.4	1	9	0	16024.7	16171.2	0.9	0	9	2	19697.5	19581.5	0.6

TABLE IV. Comparing the determined energies with the highly precise values from [30].

couplings at multi-dimensional conical intersections with residual interactions from the potential surfaces that were neglected in the separable one-dimensional potentials.

To conclude, it is fair to say that there still remains a lot to be done. How the new simplified framework of treating multi-dimensional nuclear dynamics can indeed be utilized to predict realistic laser-induced molecular dynamics as well as to provide simple interpretation of the underlying mechanism are yet to be demonstrated. Without taking such a step, on the other hand, it is difficult to expect that one can indeed understand dynamics for a complex molecule.

### ACKNOWLEDGMENTS

This research was supported in part by the Chemical Sciences, Geosciences, and Biosciences Division, Office of

Basic Energy Sciences, Office of Science, US Department of Energy, under Grant No. DE-FG02-86ER13491.

### Appendix A: Atomic displacements in $\gamma$ -set

Position of the hydrogen atoms  $\mathbf{R}_1$ ,  $\mathbf{R}_2$  and the center of mass of the molecule  $\mathbf{R}_{\text{CM}}$  is shown in Fig. 12 and the vectors can be linked to the Jacobi vectors as

$$\begin{aligned} \mathbf{R}_1 &= -\mathbf{\rho}_2 - \frac{\mu_1}{m_H} \mathbf{\rho}_1 = -\mathbf{\rho}_2 - \frac{\boldsymbol{\rho}_1}{2}, \\ \mathbf{R}_2 &= -\mathbf{\rho}_2 + \frac{\mu_1}{m_H} \mathbf{\rho}_1 = -\mathbf{\rho}_2 + \frac{\boldsymbol{\rho}_1}{2}, \\ \mathbf{R}_{\text{CM}} &= \frac{m_O}{2m_H + m_O} \mathbf{\rho}_2 = \frac{\mu_2}{4\mu_1} \mathbf{\rho}_2. \end{aligned} \quad (\text{A1})$$

The size of the Jacobi vectors is related to the hyper-

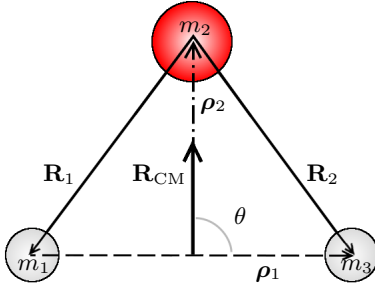


FIG. 12. Definition of Jacobi vectors  $\rho_1$  and  $\rho_2$  and their mutual angle  $\theta$  in  $\gamma$ -set and the molecular bond vectors  $\mathbf{R}_1$  and  $\mathbf{R}_2$ . The center-of-mass of the whole molecule is located at  $\mathbf{R}_{\text{CM}}$ .

spherical coordinates  $R$  and  $\phi$  via

$$\begin{aligned}\rho_1 &= \sqrt{\frac{\mu}{\mu_1}} \frac{R}{\sqrt{1 + \tan^2 \phi}}, \\ \rho_2 &= \sqrt{\frac{\mu}{\mu_2}} \frac{R \tan \phi}{\sqrt{1 + \tan^2 \phi}}.\end{aligned}\quad (\text{A2})$$

The variables  $\rho_1$  and  $\rho_2$  are interconnected with respect to derivation

$$\begin{aligned}\frac{d\rho_1}{dR} &= \frac{\rho_1}{R}, \quad \frac{d\rho_1}{d\phi} = -\sqrt{\frac{\mu_2}{\mu_1}} \rho_2, \\ \frac{d\rho_2}{dR} &= \frac{\rho_2}{R}, \quad \frac{d\rho_2}{d\phi} = +\sqrt{\frac{\mu_1}{\mu_2}} \rho_1.\end{aligned}\quad (\text{A3})$$

It is possible to show that

$$\begin{aligned}\frac{\mathbf{R}_{1,2} \cdot \partial_R \mathbf{R}_{1,2}}{|\mathbf{R}_{1,2}| |\partial_R \mathbf{R}_{1,2}|} &= 1, \\ \frac{\tilde{\mathbf{R}}_{1,2} \cdot \partial_R \tilde{\mathbf{R}}_{1,2}}{|\tilde{\mathbf{R}}_{1,2}| |\partial_R \tilde{\mathbf{R}}_{1,2}|} &= 1,\end{aligned}\quad (\text{A4})$$

where  $\tilde{\mathbf{R}}_{1,2} = \mathbf{R}_{1,2} - \mathbf{R}_{\text{CM}}$ . Neither of the remaining displacement vectors  $\partial_\phi \mathbf{R}_{1,2}$ ,  $\partial_\phi \tilde{\mathbf{R}}_{1,2}$ ,  $\partial_\theta \mathbf{R}_{1,2}$  and  $\partial_\theta \tilde{\mathbf{R}}_{1,2}$  is generally parallel or perpendicular to the vector  $\mathbf{R}_{1,2}$  or  $\tilde{\mathbf{R}}_{1,2}$  and their mutual angles are given by rather complicated and not much enlightening relations depending only on angles  $\phi$ ,  $\theta$  and masses  $\mu_1$ ,  $\mu_2$  and  $\mu$ . The displacement vectors with respect to individual coordinates can be at equilibrium, i.e.,  $\theta = 90^\circ$ , expressed for change

in hyperradius  $R$  as

$$\begin{aligned}\partial_R \mathbf{R}_1 &= \frac{1}{2R} (-\rho_1, 0, -2\rho_2), \\ \partial_R \mathbf{R}_2 &= \frac{1}{2R} (+\rho_1, 0, -2\rho_2), \\ \partial_R \mathbf{R}_{\text{CM}} &= \frac{\mu_2 \rho_2}{4\mu_1 R} (0, 0, 1),\end{aligned}\quad (\text{A5})$$

in hyperangle  $\phi$  as

$$\begin{aligned}\partial_\phi \mathbf{R}_1 &= \left( +\sqrt{\frac{\mu_2}{\mu_1}} \frac{\rho_2}{2}, 0, -\sqrt{\frac{\mu_1}{\mu_2}} \rho_1 \right), \\ \partial_\phi \mathbf{R}_2 &= \left( -\sqrt{\frac{\mu_2}{\mu_1}} \frac{\rho_2}{2}, 0, -\sqrt{\frac{\mu_1}{\mu_2}} \rho_1 \right), \\ \partial_\phi \mathbf{R}_{\text{CM}} &= \sqrt{\frac{\mu_2}{\mu_1}} \frac{\rho_1}{4} (0, 0, 1),\end{aligned}\quad (\text{A6})$$

and in hyperangle  $\theta$  as

$$\begin{aligned}\partial_\theta \mathbf{R}_1 &= \frac{\rho_1}{2} (0, 0, +1), \\ \partial_\theta \mathbf{R}_2 &= \frac{\rho_1}{2} (0, 0, -1), \\ \partial_\theta \mathbf{R}_{\text{CM}} &= \frac{\mu_2 \rho_2}{4\mu_1} (0, 0, 1).\end{aligned}\quad (\text{A7})$$

The upper results at the equilibrium can be used to construct the character table of the displacements and compare those with the of the normal modes in Table V.

$\text{C}_{2\nu}$	E	$\text{C}_2$	$\sigma(xy)$	$\sigma(yz)$
$\nu_1$	1	1	1	1
$\nu_2$	1	1	1	1
$\nu_3$	1	-1	-1	1
<hr/>				
$\nu_R$	1	1	1	1
$\nu_\phi$	1	1	1	1
$\nu_\theta$	1	-1	-1	1

TABLE V. Character table for the normal modes ( $\nu_1$ ,  $\nu_2$ ,  $\nu_3$ ) and hyperspherical modes ( $\nu_R$ ,  $\nu_\phi$ ,  $\nu_\theta$ ) of a water molecule.

Nevertheless, displacement in the individual hyperspherical coordinates are strictly speaking not the well-known normal modes since the kinetic part of the Hamiltonian in Eq. (9) is not separable in the hyperangular part.

---

[1] A. Trabattoni, M. Klinker, J. González-Vázquez, C. Liu, G. Sansone, R. Linguerri, M. Hochlaf, J. Klei, M. J. J. Vrakking, F. Martín, M. Nisoli, and F. Calegari, “Mapping the dissociative ionization dynamics of molecular nitrogen with attosecond time resolution,” *Phys. Rev. X*, vol. 5, p. 041053, Dec 2015.

[2] F. Krausz and M. Ivanov, “Attosecond physics,” *Rev. Mod. Phys.*, vol. 81, pp. 163–234, Feb 2009.

[3] M. Nisoli, P. Decleva, F. Calegari, A. Palacios, and F. Martín, “Attosecond electron dynamics in molecules,” *Chemical Reviews*, vol. 117, no. 16, pp. 10760–10825, 2017. PMID: 2848433.

[4] W. Demtröder, *Atoms, Molecules and Photons*. Springer Berlin Heidelberg New York, 2006. An optional note.

[5] L. Halonen and T. Carrington, “Fermi resonances and local modes in water, hydrogen sulfide, and hydrogen se-

lenide," *The Journal of Chemical Physics*, vol. 88, no. 7, pp. 4171–4185, 1988.

[6] B. T. Darling and D. M. Dennison, "The water vapor molecule," *Phys. Rev.*, vol. 57, pp. 128–139, Jan 1940.

[7] K. Kuchitsu and L. S. Bartell, "Effect of anharmonic vibrations on the bond lengths of polyatomic molecules. i. model of force field and application to water," *The Journal of Chemical Physics*, vol. 36, no. 9, pp. 2460–2469, 1962.

[8] M. S. Child and L. Halonen, *Overtone Frequencies and Intensities in the Local Mode Picture*, pp. 1–58. John Wiley & Sons, Ltd, 2007.

[9] M. Carleer, A. Jenouvrier, A.-C. Vandaele, P. F. Bernath, M. F. Mrienne, R. Colin, N. F. Zobov, O. L. Polyansky, J. Tennyson, and V. A. Savin, "The near infrared, visible, and near ultraviolet overtone spectrum of water," *The Journal of Chemical Physics*, vol. 111, no. 6, pp. 2444–2450, 1999.

[10] S. E. Choi and J. C. Light, "Highly excited vibrational eigenstates of nonlinear triatomic molecules. application to  $\text{H}_2\text{O}$ ," *The Journal of Chemical Physics*, vol. 97, no. 10, pp. 7031–7054, 1992.

[11] J. Manz and H. Schor, "Hyperspherical modes," *Chemical Physics Letters*, vol. 107, no. 6, pp. 542 – 548, 1984.

[12] A. Bastida, J. Zúñiga, A. M. Molina, and A. Requena, "Vibrational self-consistent-field approximation for triatomic molecules using hyperspherical modes with application to  $\text{H}_2\text{O}$ ," *International Journal of Quantum Chemistry*, vol. 42, no. 3, pp. 475–488, 1992.

[13] T. Joseph, T.-M. Kruel, J. Manz, and I. Rexrodt, "Model calculation of local versus hyperspherical mode selective dissociation of  $\text{H}_2\text{O}$ ," *Chemical Physics*, vol. 113, no. 2, pp. 223 – 230, 1987.

[14] B. Hartke, J. Manz, and J. Mathis, "Mode selective control of unimolecular dissociations: Survey, and model simulations for  $\text{HDO} \rightarrow \text{H}+\text{DO}$ ,  $\text{D}+\text{HO}$ ," *Chemical Physics*, vol. 139, no. 1, pp. 123 – 146, 1989.

[15] B. Hartke and J. Manz, "A new quantum isotope effect: Extreme local mode selectivity in unimolecular dissociations imposed by antagonism between dynamic propensities of educts and zero point energies of products," *The Journal of Chemical Physics*, vol. 92, no. 1, pp. 220–226, 1990.

[16] B. Hartke, A. E. Janza, W. Karrlein, J. Manz, V. Mohan, and H. Schreier, "Local versus hyperspherical modes of water and formaldehyde: Effect of molecular complexity on modeselective structures and dynamics," *The Journal of Chemical Physics*, vol. 96, no. 5, pp. 3569–3584, 1992.

[17] B. R. Johnson and W. P. Reinhardt, "Adiabatic separations of stretching and bending vibrations: Application to  $\text{H}_2\text{O}$ ," *The Journal of Chemical Physics*, vol. 85, no. 8, pp. 4538–4556, 1986.

[18] B. J. Rosenberg, W. C. Ermler, and I. Shavitt, "Ab initio scf and ci studies on the ground state of the water molecule. ii. potential energy and property surfaces," *The Journal of Chemical Physics*, vol. 65, no. 10, pp. 4072–4080, 1976.

[19] A. J. Dobbyn and P. J. Knowles, "A comparative study of methods for describing non-adiabatic coupling: diabatic representation of the 1sigma +/1pi hoh and hho conical intersections," *Molecular Physics*, vol. 91, no. 6, pp. 1107–1124, 1997.

[20] R. van Harreveld and M. C. van Hemert, "Photodissociation of water. i. electronic structure calculations for the excited states," *The Journal of Chemical Physics*, vol. 112, no. 13, pp. 5777–5786, 2000.

[21] O. L. Polyansky, A. G. Császár, S. V. Shirin, N. F. Zobov, P. Barletta, J. Tennyson, D. W. Schwenke, and P. J. Knowles, "High-accuracy ab initio rotation-vibration transitions for water," *Science*, vol. 299, no. 5606, pp. 539–542, 2003.

[22] P. Barletta, S. V. Shirin, N. F. Zobov, O. L. Polyansky, J. Tennyson, E. F. Valeev, and A. G. Csszr, "Cvqrqd ab initio ground-state adiabatic potential energy surfaces for the water molecule," *The Journal of Chemical Physics*, vol. 125, no. 20, p. 204307, 2006.

[23] S. V. Shirin, N. F. Zobov, R. I. Ovsyannikov, O. L. Polyansky, and J. Tennyson, "Water line lists close to experimental accuracy using a spectroscopically determined potential energy surface for  $\text{H}_2\text{O}^{16}$ ,  $\text{H}_2\text{O}^{17}$ , and  $\text{H}_2\text{O}^{18}$ ," *The Journal of Chemical Physics*, vol. 128, no. 22, p. 224306, 2008.

[24] I. I. Bubukina, N. F. Zobov, O. L. Polyansky, S. V. Shirin, and S. N. Yurchenko, "Optimized semiempirical potential energy surface for  $\text{H}_2^{16}\text{O}$  up to 26000  $\text{cm}^{-1}$ ," *Optics and Spectroscopy*, vol. 110, pp. 160–166, Feb 2011.

[25] B. Jiang, D. Xie, and H. Guo, "Communication: State-to-state differential cross sections for  $\text{H}_2\text{O}(\text{b})$  photodissociation," *The Journal of Chemical Physics*, vol. 134, no. 23, p. 231103, 2011.

[26] B. Jiang, D. Xie, and H. Guo, "State-to-state photodissociation dynamics of triatomic molecules:  $\text{H}_2\text{O}$  in the b band," *The Journal of Chemical Physics*, vol. 136, no. 3, p. 034302, 2012.

[27] O. L. Polyansky, A. A. Kyuberis, N. F. Zobov, J. Tennyson, S. N. Yurchenko, and L. Lodi, "ExoMol molecular line lists XXX: a complete high-accuracy line list for water," *Monthly Notices of the Royal Astronomical Society*, vol. 480, pp. 2597–2608, 08 2018.

[28] P. Jensen, "The potential energy surface for the electronic ground state of the water molecule determined from experimental data using a variational approach," *Journal of Molecular Spectroscopy*, vol. 133, no. 2, pp. 438 – 460, 1989.

[29] C. Lin, "Hyperspherical coordinate approach to atomic and other coulombic three-body systems," *Physics Reports*, vol. 257, no. 1, pp. 1 – 83, 1995.

[30] J. J. S. Neto and L. S. Costa, "Numerical generation of optimized discrete variable representations," *Brazilian Journal of Physics*, vol. 28, pp. 1–11, Mar 1998.

[31] J. Tennyson and B. T. Sutcliffe, "The ab initio calculation of the vibrationalrotational spectrum of triatomic systems in the closecoupling approach, with  $\text{KCN}$  and  $\text{H}_2\text{Ne}$  as examples," *The Journal of Chemical Physics*, vol. 77, no. 8, pp. 4061–4072, 1982.

[32] C.-N. Liu, A.-T. Le, T. Morishita, B. D. Esry, and C. D. Lin, "Hyperspherical close-coupling calculations for charge-transfer cross sections in  $\text{He}^{2+} + \text{H}(1s)$  collisions at low energies," *Phys. Rev. A*, vol. 67, p. 052705, May 2003.

[33] A. Hoy, I. Mills, and G. Strey, "Anharmonic force constant calculations," *Molecular Physics*, vol. 24, no. 6, pp. 1265–1290, 1972.

[34] A. F. Starace and G. L. Webster, "Atomic hydrogen in a uniform magnetic field: Low-lying energy levels for fields below  $10^9$  g," *Phys. Rev. A*, vol. 19, pp. 1629–1640, Apr 1979.

- [35] B. D. Esry, C. D. Lin, and C. H. Greene, “Adiabatic hyperspherical study of the helium trimer,” *Phys. Rev. A*, vol. 54, pp. 394–401, Jul 1996.
- [36] H. Bachau, E. Cormier, P. Decleva, J. E. Hansen, and F. Martín, “Applications of B-splines in atomic and molecular physics,” *Reports on Progress in Physics*, vol. 64, pp. 1815–1943, nov 2001.